

On radar imaging of current features: 2. Mesoscale eddy and current front detection

J. A. Johannessen,^{1,2} V. Kudryavtsev,^{3,4} D. Akimov,³ T. Eldevik,^{1,5}
N. Winther,¹ and B. Chapron⁶

Received 12 November 2004; revised 17 March 2005; accepted 12 April 2005; published 22 July 2005.

[1] The surface signatures of meandering fronts and eddies have been regularly observed and documented in synthetic aperture radar (SAR) images. Wave-current interactions, the suppression of short wind waves by natural film, and the varying wind field resulting from atmospheric boundary layer changes across an oceanic temperature front all contribute to the radar image manifestation of such mesoscale features. The corresponding imaging mechanisms are quantitatively explored using a new radar imaging model (Kudryavtsev et al., 2005) that solves the energy balance equation where wind forcing, viscous and wave breaking dissipation, wave-wave interactions, and generation of short waves by breaking waves are taken into account. High-quality and synoptic in situ observations of the surface conditions should ideally be used in this model. However, such data are rarely available. Instead, the fields of temperature and ocean current are herein derived from two distinct numerical ocean models. SAR image expressions of current fronts and eddies are then simulated based on these fields. The comparison of simulated images with European Remote Sensing (ERS) SAR and Envisat advanced SAR (ASAR) images is favorable. We consequently believe that the new radar imaging model provides promising capabilities for advancing the quantitative interpretation of current features manifested in SAR images.

Citation: Johannessen, J. A., V. Kudryavtsev, D. Akimov, T. Eldevik, N. Winther, and B. Chapron (2005), On radar imaging of current features: 2. Mesoscale eddy and current front detection, *J. Geophys. Res.*, 110, C07017, doi:10.1029/2004JC002802.

1. Introduction

[2] Upper ocean fronts and eddies are dynamic features that importantly contribute to the mesoscale variability, the coupled physical-biochemical processes, and rapid changes in the air-sea interaction. Such features are usually manifested by the sea surface temperature pattern and chlorophyll *a* concentration in thermal infrared and visible satellite remote sensing images. In synthetic aperture radar (SAR) images they are manifested owing to sea surface roughness changes [e.g., *Fu and Stewart*, 1983; *Alpers*, 1985; *Johannessen et al.*, 1996; *Lyzenga*, 1996; *Johannessen et al.*, 1997; *Font et al.*, 2002; *Lyzenga et al.*, 2004]. Quantitative analyses of current strength and variability connected with such remotely sensed features are not trivial and hitherto mostly limited to simplified cases. A major

reason for this, in particular regarding SAR images, is the complex interplay between physical processes and the challenging demand for coincident high quality in situ data. Ideally, this should include observations of the surface wind field, surface waves, surface current, and presence of damping surfactant material. In addition, knowledge of the changes in the atmospheric boundary layer stratification and thus surface stress in the presence of a sea surface temperature front are also required. The availability of such a range of coincident data at high spatial resolution is extremely rare.

[3] Consequently, there is a lack of systematic use of SAR images for studies of frontal features and their impact on the mesoscale variability of current systems such as the Gulf Stream and coastal boundary currents. However, the fundamental equations for SAR imaging of surface current features have gradually become better known [*Alpers and Hennings*, 1984; *Lyzenga and Bennett*, 1988; *Apel*, 1994; *Romeiser and Alpers*, 1997; *Romeiser et al.*, 2001; *Kudryavtsev et al.*, 2005] and can now be applied to simulate SAR image expressions. Figure 1 schematically outlines the main steps of the new radar imaging model (RIM) by *Kudryavtsev et al.* [2005] (hereinafter referred to as Part 1). On the basis of detailed quantitative characterization of the surface current, the near-surface wind field, and the presence of surfactants, the conservation of wave action (i.e., energy balance) is invoked to consistently describe the surface roughness modulations. The roughness

¹Nansen Environmental and Remote Sensing Center, Bergen, Norway.

²Also at Geophysical Institute, University of Bergen, Bergen, Norway.

³Nansen International Environmental and Remote Sensing Center, St. Petersburg, Russia.

⁴Also at Marine Hydrophysical Institute, Sebastopol, Ukraine.

⁵Also at Bjerknes Center for Climate Research, Bergen, Norway.

⁶Institute Français de Recherche pour l'Exploitation de la Mer, Plouzane, France.

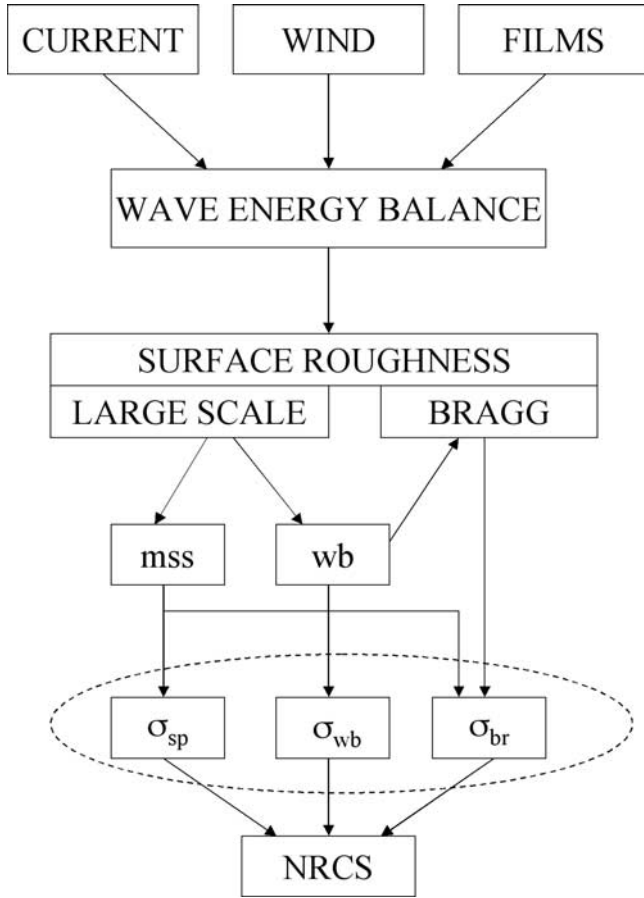


Figure 1. Schematic illustration of the main radar imaging model assumptions and principles. Note that the sea surface roughness is an integral from the large-scale tilt that determines mean square slope (mss) and breaking waves (wb) to the small-scale Bragg (br) wavelengths. The three terms that contribute to the normalized radar cross section (NRCS) are quasi-specular contribution σ_{sp} , impact from breaking waves σ_{wb} , and Bragg scattering σ_{br} .

is partitioned into larger-scale waves and small-scale Bragg waves. The mean square slope (mss) of larger-scale waves contributes directly to specular reflection (sp), but also to Bragg (br) scattering by means of the tilting of shorter waves. In addition, wave breaking (wb) of larger-scale waves alters the surface roughness and generates smaller-scale Bragg waves. In turn, the total surface scattering properties can be quantified and used to simulate the normalized radar cross section (NRCS) applicable to real aperture radar imaging.

[4] In this paper, the demand for high-quality in situ validation data is bypassed by the alternative use of surface fields of temperature and current derived from numerical ocean models. The models are a fine resolution (650 m) process model [Eldevik and Dysthe, 2002] and an operational model of the Norwegian Coastal Current (NCC) at 2–4 km resolution [Bertino et al., 2004; Albretsen et al., 2004]. These model data are used to feed the RIM of Part 1. In section 2 we briefly describe the major steps of the RIM, while the imaging of frontal eddies is simulated and compared with SAR images in section 3. Building on this,

the SAR imaging of coastal current features is simulated in section 4 followed by a comparison with SAR observations. A summary with concluding remarks is then provided in section 5.

2. SAR Signatures of Surface Current Features

2.1. Major Steps of the RIM

[5] As discussed and highlighted in Part 1, the RIM provides consistent insight into the physics responsible for the image manifestation of surface current features building on work by Kudryavtsev et al. [2003a, 2003b]. In the following, we briefly outline the RIM (Figure 1) in Part 1, where a module for surface roughness estimation is combined with a module for predicting the NRCS for VV- and HH-polarization (p). The latter accounts for the Bragg scattering (σ_{br}^p , two-scale model), the quasi-specular contribution (σ_{sp}) and the impact from breaking waves (σ_{wb}) such that the NRCS is given by

$$\sigma_0^p = (\sigma_{br}^p + \sigma_{sp})(1 - q) + \sigma_{wb}q, \quad (1)$$

where q is the fraction of the sea surface covered by breaking waves. These three scattering mechanisms depend on the radar wavelength, polarization, and incidence angle. Within the frame of the composite model, the range of longer surface waves providing tilt and specular contribution is defined as $k < d \cdot k_r$, where k_r is the radar wave number and $d = 1/4$ is the dividing parameter. The main characteristics of longer waves contributing to σ_{br}^p and defining σ_{sp} are their mss in up- and cross-wind directions (s_1^2 and s_2^2 , respectively), which are related to the dimensionless saturation spectrum $B(k)$ of wind waves as

$$s_j^2 = \int_{k < dk_r} \kappa_j^2 k^{-2} B(\mathbf{k}) dK, \quad (2a)$$

where κ_j is a component of the unit wave number vector directed with an angle ϕ relative to the wind direction, and $dK = kdkd\phi$.

[6] The impact of wave breaking is described as the integrated effect of steep patches of breaking waves that contribute to the radar return (σ_{wb}) by reflection. This contribution is proportional to the fraction of the sea surface q covered by breaking zones. This quantity, as well as the energy dissipation from wave breaking, is described using the wave breaking characteristics originally introduced by Phillips [1985]. As shown in Part 1, q can then be expressed via the saturation spectrum B and wind wave growth rate β as

$$q = c_q \int \int_{k < k_{wb}} \beta (B + (n_g + 1)\tilde{B}) d\varphi d \ln k, \quad (2b)$$

where c_q is a constant, $\beta = C_\beta (u_* / c)^2 \cos \varphi |\cos \varphi|$, and $n_g = 5$ is a parameter related to the choice of spectral dissipation. Hereinafter, tilde denotes the variation of any quantity with respect to the background values. The β attains negative values for waves propagating at more than 90° to the wind direction. In such cases, the wind waves attenuate and lose their energy interacting with the opposing wind [Lyzenga, 1996; Kudryavtsev and Johannessen, 2004].

[7] The spectrum of Bragg waves, waves defining the mss (equation (2a)), and the wave breaking (equation (2b)) that in total contribute to the NRCS (σ_o^p) are all found by solving the wave energy conservation equation in the roughness module of the RIM. For any small roughness disturbances, the wave action N conservation equation (per unit mass) reads

$$\begin{aligned} & \partial \tilde{N}(\mathbf{k}) / \partial t + c_{gi} \partial \tilde{N}(\mathbf{k}) / \partial x_i \\ & = \omega^2 k^{-5} [\omega^{-1} m_k^{ij} u_{i,j} B_0 - \tilde{B} / \tau + \tilde{\beta} B_0 + \tilde{I}_{sw}], \end{aligned} \quad (3)$$

where c_{gi} and $u_{i,j}$ are the wave group velocity and surface current velocity gradient tensor $\partial u_i / \partial x_j$ (i and $j = 1, 2$), τ is a dimensionless relaxation time, and ω and \mathbf{k} are the intrinsic frequency and wave number vector (with components k_i) related by the dispersion relation

$$\omega^2 = gk + \gamma k^3. \quad (4)$$

[8] In the above, $k = |\mathbf{k}|$, g is the acceleration of gravity, and γ is the surface tension. B_0 is defining the background spectrum. The saturation spectrum B relates to N as $N(\mathbf{k}) = \omega k^{-5} B(\mathbf{k})$, $m_k^{ij} = k_j \partial \ln N_0 / \partial k_i$ is a tensor of the ‘‘wave number exponent’’ of the spectrum, $\tilde{\beta}$ represents the variations in wind wave growth rate which are proportional to the wind surface stress variations, and \tilde{I}_{sw} is the rate of short wave modulations due to the modulation by the breaking of the longer, intermediate waves,

$$\tilde{I}_{sw}(k) = \frac{c_b}{2\alpha} \omega^{-1} (n_g + 1) \int \int_{k < k_m} \omega \tilde{\beta} d \ln k d\varphi, \quad (5)$$

where c_b is a constant and α as given by Kudryavtsev *et al.* [2003a]. The operator $m_k^{ij} u_{i,j}$ is

$$\begin{aligned} m_k^{ij} u_{i,j} & = m_k (\cos^2 \varphi \cdot (u_{1,1} + u_{2,2}) - \cos 2\varphi \cdot u_{2,2}) + 1/2 m_\varphi \sin 2\varphi \\ & \cdot (u_{2,2} - u_{1,1}) + 1/2 m_k \sin 2\varphi \cdot (u_{2,1} + u_{1,2}) \\ & - m_\varphi (\sin^2 \varphi \cdot u_{2,1} - \cos^2 \varphi \cdot u_{1,2}), \end{aligned} \quad (6)$$

where

$$m_k = \partial \ln N / \partial \ln k, \quad m_\varphi = \partial \ln N / \partial \varphi.$$

[9] Both the surface current and the near-surface wind are considered stationary in the simulations. If we assume that the spatial scale of the surface current L is larger than the relaxation scale $l_r = \omega^{-1} \tau c_g$, then the advective term on the left hand side of equation (3) can be ignored, and the equation reduces to

$$\tilde{B}(\mathbf{k}) / B_0(\mathbf{k}) = \tau \left(\omega^{-1} m_k^{ij} u_{i,j} + 2\tilde{\beta} \tilde{u}_* / u_* + \tilde{I}_{sw} / B_0 \right). \quad (7)$$

[10] This expression clearly emphasizes the role of the main mechanisms responsible for the surface roughness modulations: surface current gradients (first term), varying surface wind stress (second term), and wave breaking from intermediate waves (third term). The effect of surfactants is also included in the background spectrum B_0 through the effective molecular viscosity coefficient (see Part 1). Notice

that the contribution from wave breaking to shorter roughness scale modulations is a salient feature of the proposed model. Indeed, the direct effect of current changes to short waves is negligible owing to the weak relaxation rate. Thus the roughness modulation by intermediate wave breaking appears as the dominant source in the presence of a current. This source is mostly isotropic, and the relaxation time τ takes larger values at cross-wind directions. Hence wave-current interactions and subsequent wave breaking, notably more intense for the intermediate waves, result in more isotropic surface roughness [Kudryavtsev and Johannessen, 2004].

[11] As already emphasized in Part 1, a varying surface stress results from changes in the atmospheric boundary layer across a sea surface temperature front. In passing from the relatively colder to the warmer side, the atmospheric stratification might become less stable. In turn, the surface stress increases and roughness modulations are produced.

[12] Among the different components of the surface current gradient tensor, the dominant contribution is mostly related to effects of convergence and divergence. Indeed, the variations in the mean square slope and wave breaking as well as Bragg wave modulations (via the intermediate scale wave breaking mechanism) are all strongly affected by such current gradients. Assuming that the x_1 axis is aligned with the wind, the integral of $m_k^{ij} u_{i,j}$ multiplied by any even function (e.g., B or β) over φ is zero. If the function has a wide angular spreading (like B in the equilibrium gravity range), then the main contribution to the integrals over φ comes from the first term in equation (6), and the operator may be approximated by

$$m_k^{ij} u_{i,j} \approx m_k \nabla \cdot \mathbf{u}. \quad (8)$$

[13] The breaking of intermediate waves in the equilibrium range, where the angular spreading of the spectrum is wide, mainly causes the fraction of the sea surface covered by enhanced roughness zones. Consequently, enhancement and suppression of surface roughness occur in the zones of convergence and divergence, respectively.

[14] Interestingly, surfactants also tend to accumulate in the zones of the current convergence to dampen short wind waves. The effects of pure wave-current interaction and surfactant damping may then lead to opposite radar signatures for current convergence areas. It is reasonable to anticipate that the resulting net effect depends on the wind conditions, the magnitude of the current convergence and the properties of any surfactant material present.

2.2. RIM Sensitivity

[15] To illustrate and quantify these different SAR imaging effects, a series of basic RIM simulations for C-band radars are presented assuming two simple linear current fields:

(1) convergent current,

$$u_1(x_1) = -u_{01} F(x_1/L), \quad u_2 = 0, \quad (9)$$

and (2) shear current,

$$u_1 = 0, \quad u_2(x_1) = u_{02} F(x_1/L), \quad (10)$$

where the profile function takes the form $F(x) = (1 + \tanh(x))/2$. Across the current front (assumed to have a width of

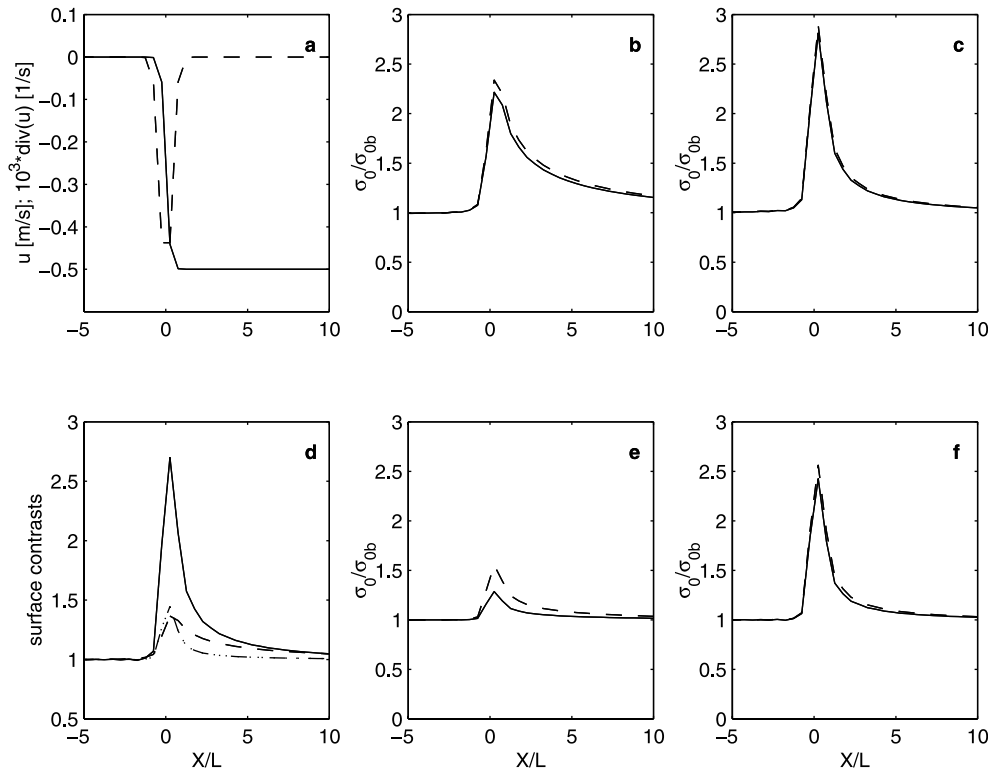


Figure 2. Model response for the convergent front in x_1 -direction. (a) Current velocity component perpendicular to the front (solid line); current divergence (dashed line). (b) NRCS contrasts for C-band at 20° incidence angle, VV (solid line) and HH (dashed line) polarizations for down-wind radar look direction. (c) Same as Figure 2b but for cross-wind radar look direction. (d) Relative contribution to the contrasts for white caps coverage (solid line), mean square slope (dashed line), and Bragg waves spectrum (dash-dotted line). (e) Same as for Figure 2b but for 40° incidence angle. (f) Same as Figure 2e but for cross-wind radar look direction.

$L = 250$ m starting from $x_1 = 0$) the x - and y -components of the current increase from 0 to $u_{01} = u_{02} = 0.5$ m/s at $x_1 = 250$ (Figure 2a). The corresponding current convergence and positive shear thus reach a maximum of $0.4 \times 10^{-3} \text{ s}^{-1}$.

[16] Figures 2b–2f illustrate the RIM results for the convergent current assuming a wind speed of 5 m/s directed along the x_1 axis. The peak over background (POB) ratio of the NRCS at VV and HH polarization, for the down- and cross-wind radar look directions and for the two incidence angles $\theta = 20^\circ$ and $\theta = 40^\circ$, are plotted. At an incidence angle of 20° , the POB ratio for the cross-wind direction is 2.7 and slightly larger compared to the down-wind direction at about 2.3 (Figures 2b and 2c). The magnitude and shape of the HH and VV polarizations have no distinct differences for the two cases. In the vicinity of maximum convergence the wave breaking is significantly enhanced compared to the background level (Figure 2d). The mean square slope and omni-directional spectrum of Bragg waves are also intensified in the convergence zone, although the magnitudes of their modulations are much less pronounced (Figure 2d). At $\theta = 40^\circ$ the POB ratio for HH polarization is markedly higher than for VV but clearly less than at $\theta = 20^\circ$ (Figure 2e). This arises from the effect of wave breaking which provides a relatively stronger modulation on the radar scattering for HH as shown in Part 1. In contrast, the POB ratio for the cross-wind radar look direction case at $\theta = 40^\circ$ (Figure 2f) is in closer agreement with the results at $\theta = 20^\circ$.

The large POB ratio in this direction results from the significantly higher sensitivity of Bragg waves to surface current at cross- than at downwind radar look directions.

[17] The impact of a “pure” shear current on wind wave modulations is found to be relatively negligible and is not shown. This result seems at first to disagree with the numerous radar manifestations of current boundaries that are known to have significant shear current [i.e., Johannessen *et al.*, 1996; Lyzenga *et al.*, 2004]. Note, however, that here we only consider shear currents normal to the wind and look direction. Johannessen *et al.* [1996] have also reported that in cases with pure shear currents perpendicular to the wind and look direction the effect of the shear on the radar cross-section modulation is negligible. When shear currents, on the other hand, are neither perpendicular nor along the wind and look direction, the integral statistical properties of the sea surface roughness (see equation (8)) may experience modulations that are manifested in the SAR image.

[18] The general nonstationary nature of meandering currents, including local zones of convergence and divergence, thus explains the image manifestation of shear currents. Using the conservation of vertical vorticity (Ω_z),

$$\frac{d\Omega_z}{dt} = -(\Omega_z + f)\nabla \cdot \mathbf{u}, \quad (11)$$

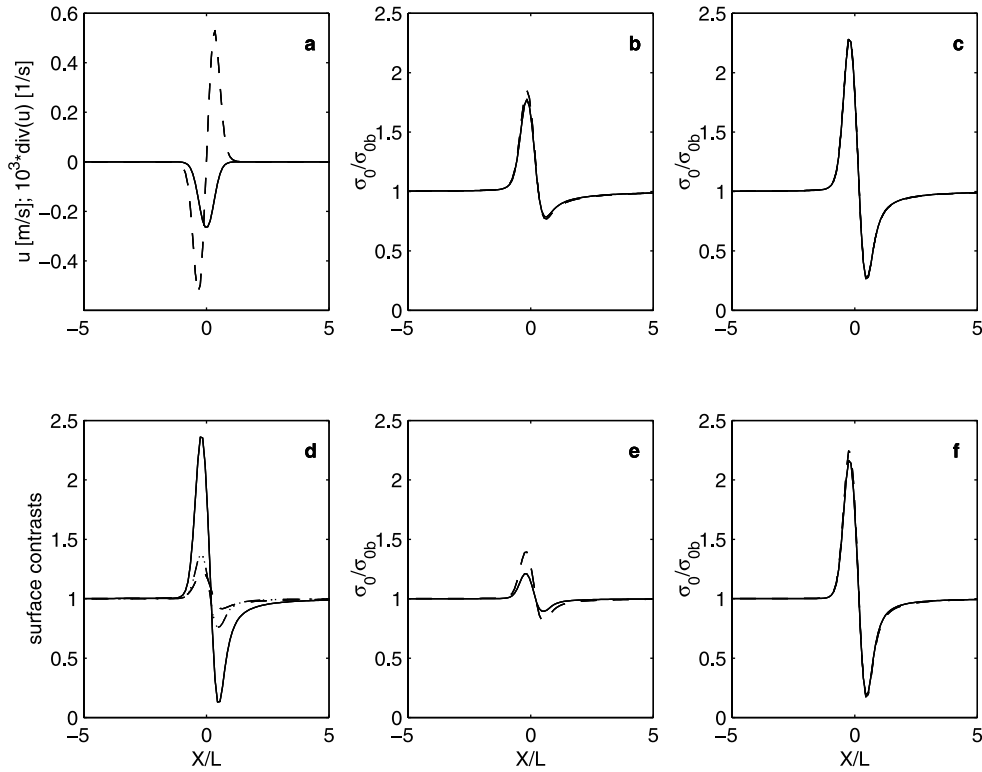


Figure 3. Model response for the meandering shear current front in x_1 direction. (a) Current velocity component perpendicular to the front (solid line); current divergence (dashed line). (b) NRCS contrasts for C-band at 20° incidence angle, VV (solid line) and HH (dashed line) polarizations for down-wind radar look direction. (c) Same as Figure 3b but for cross-wind radar look direction. (d) Relative contribution to the contrasts for white caps coverage (solid line), mean square slope (dashed line), and Bragg waves spectrum (dash-dotted line). (e) Same as for Figure 3b but for 40° incidence angle. (f) Same as Figure 3e but for cross-wind radar look direction.

(with f being the Coriolis parameter) it follows that convergence (divergence) increases (decreases) the shear. This equation predicts the existence of oscillating linear convergence and divergence zones distributed along the current shear front. For small perturbations, this is approximated by

$$\frac{\partial \zeta}{\partial t} \frac{\partial^2 u_2}{\partial x_1^2} \approx - \left(f + \frac{\partial u_2}{\partial x_1} \right) \nabla \cdot \mathbf{u}. \quad (12)$$

[19] If we allow the initial shear current to experience small oscillating meanders of size $\zeta(x_2, t) = a \cos(K(x_2 - Ct))$, with $aK \ll 1$, the shear current can be modeled as

$$u_2(x_1, x_2) = u_{02} F[(x_1 - \zeta)/L]. \quad (13)$$

[20] To model the corresponding radar signature of this meandering current, we specified $C = u_{02}/2$, $aK = 0.5$ and as before the frontal width $L = 250$ m. The corresponding divergence and convergence of the current and induced velocity component u_1 are shown in Figure 3a. The perturbation velocity of the meander perpendicular to the front exceeds 0.2 m/s, while the magnitude and shape of the convergence and divergence are symmetric at the center of the front reaching maxima of about $0.5 \times 10^{-3} \text{ s}^{-1}$.

[21] Since the direct impact of the current shear is negligible, both surface roughness contrasts and NRCS

modulations are solely caused by the convergence and divergence of the meandering shear current displayed in Figure 3a. The corresponding sensitivities of the NRCS to the same radar parameters as in Figures 2b–2f are then plotted in Figures 3b–3f. With the exception of the shape of the POB ratio the general findings and conclusions are, not surprisingly, complementing those for the pure convergence case. The effect of wave breaking in the vicinity of the maximum convergence zone dominates the contribution to the NRCS anomalies, the cross-wind radar look direction gives the largest POB ratio of about 2.3 at $\theta = 20^\circ$ and 2.2 at $\theta = 40^\circ$, and VV versus HH ratios display marked differences only at $\theta = 40^\circ$. The effects of the divergence along the shear current are specifically found for a POB ratio below 1; that is, these zones produce surface roughness less than the average background roughness. Consequently, the simulated radar signal portrays zones of bright and dark NRCS anomalies along the frontal zones. This is also commonly observed in SAR images [e.g., Johannessen *et al.*, 1996].

[22] In order to account for the effect of changes in the marine atmospheric boundary layer (MABL) on the radar imaging, the simulation is expanded to include an accompanying change in the sea surface temperature. We consider a step-like temperature front with a drop of 3°C . The MABL stratification on the up-wind side of the front is assumed to be neutral. The model simulations are in this case revealing

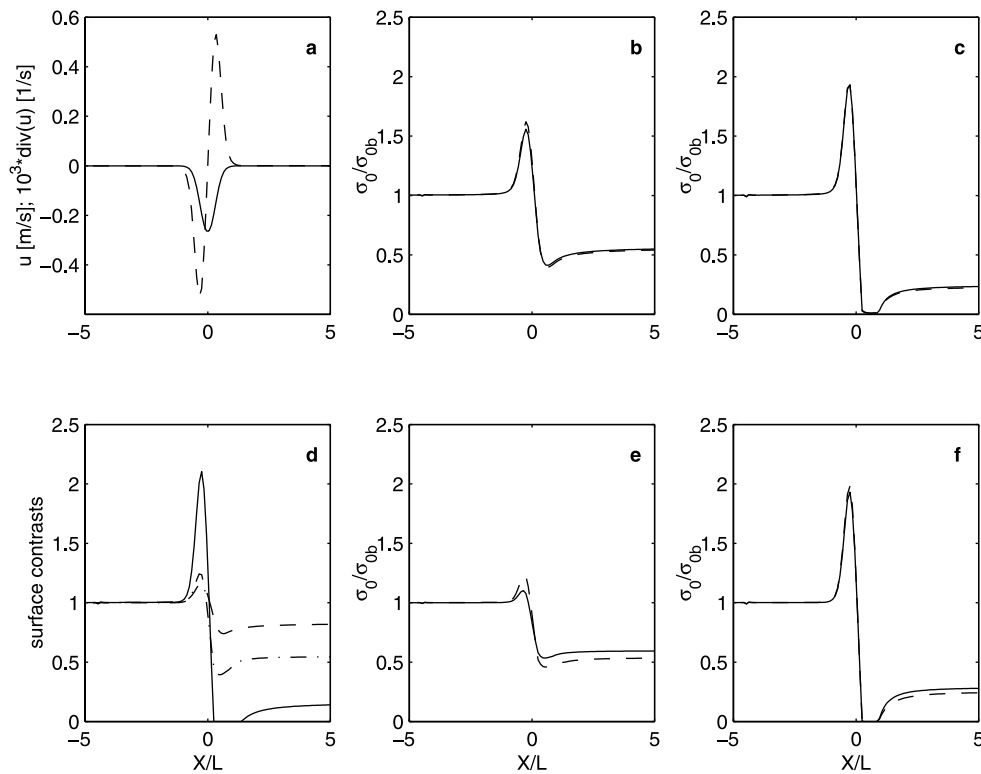


Figure 4. Model response for the meandering shear current front accompanied by a sea surface temperature front. (a) Current velocity component perpendicular to the front (solid line); current divergence (dashed line). (b) NRCS contrasts for C-band at 20° incidence angle, VV (solid line) and HH (dashed line) polarizations for down-wind radar look direction. (c) Same as Figure 4b but for cross-wind radar look direction. (d) Relative contribution to the contrasts for white caps coverage (solid line), mean square slope (dashed line), and Bragg waves spectrum (dash-dotted line). (e) Same as for Figure 4b but for 40° incidence angle. (f) Same as Figure 4e but for cross-wind radar look direction.

surface roughness changes from the combined effect of varying wind stress in the MABL (induced by the sea surface temperature front) and surface current convergence and divergence (induced by the meandering current). The results are plotted in Figures 4a–4f, using the previously specified radar parameters. The overall characteristics of these results clearly agree with the previous findings, notably regarding the importance of wave breaking in the vicinity of surface convergence, and the radar look direction. However, in this case the POB ratio distinctively remains equal to or below 0.5 on the down-wind cold and stable side of the front in contrast to the signals in Figures 2 and 3. The changes in the stratification of the MABL and subsequent wind stress changes produce a step-like drop of the surface roughness and the magnitude of the radar signal at the down-wind side of the front.

[23] The results of these RIM simulation experiments are in agreement with the comparison between modeled and observed NRCS for the CoastWatch95 experiment as reported by Kudryavtsev *et al.* [2003c] and Part 1. As found, the enhanced wave breaking in the vicinity of the surface current convergence zones explains fairly well the delta-like NRCS increase. However, such delta-like increase can gradually shift to a combined delta- and step-like change provided the joint effects of the surface current divergence and the changes in the wind stress are consid-

ered. For a given strength of convergence, the latter will therefore lead to the largest NRCS contrasts.

[24] Building on these promising 1-D sensitivity results we will in the next sections examine the capability of the RIM to simulate the 2-D imaging of frontal eddies and coastal current features. The background data of sea surface current, surface temperature, and wind speed to be fed into the RIM are entirely taken from 3-D numerical ocean models, sidestepping the problem of lacking in situ data.

3. Frontal Eddies

[25] The upper ocean is rich in mesoscale structures such as fronts and eddies. A distinct example is the so-called spiral eddies. They are rather intense surface layer cyclones with a diameter of about 10 km. Photographs of the world oceans from space shuttles [Scully-Power, 1986; Munk *et al.*, 2000], and images of Norwegian coastal waters from radar satellites [Dokken and Wahl, 1996; Johannessen *et al.*, 1996], have shown that such eddies are common. A street of spiral eddies is shown in Figure 5a. The bright lines are narrow bands of surface film (slicks) that dampen short gravity-capillary waves to produce sun glitter. Their signature is the opposite in radar images as such surfactant material suppresses the radar backscatter leading to narrow dark bands as illustrated in the SAR image (Figure 5b).

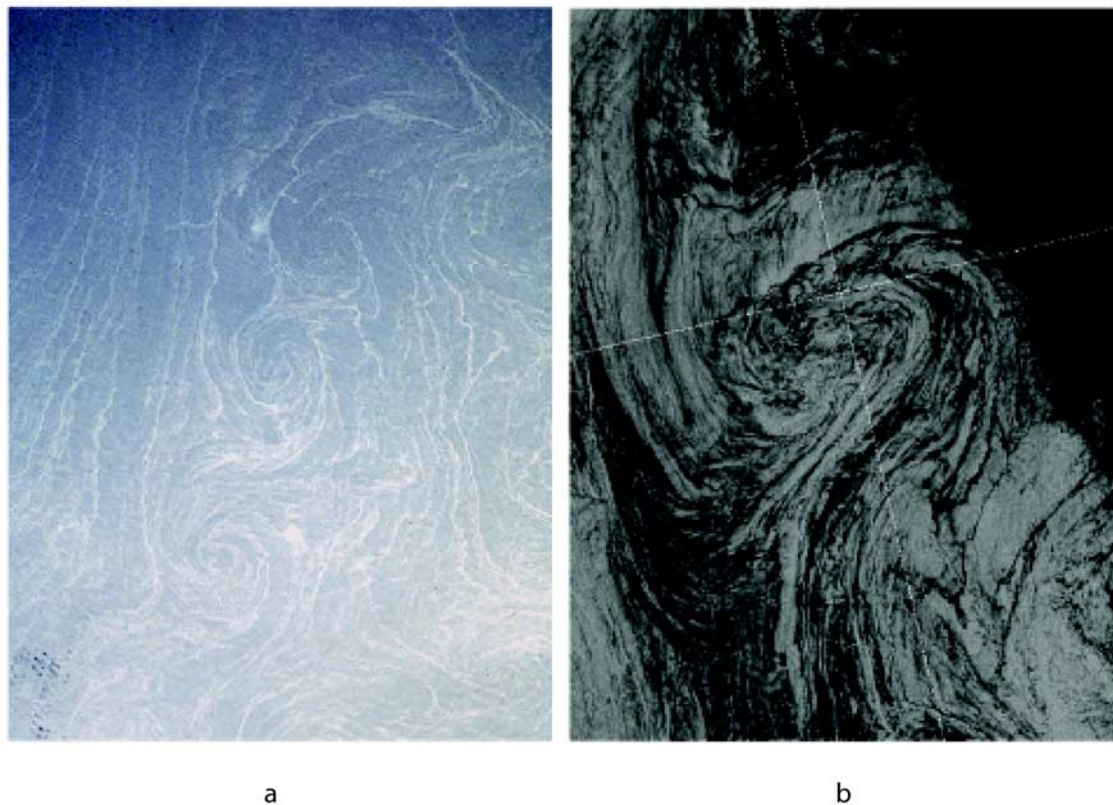


Figure 5. (a) Photograph of a spiral eddy street in the Mediterranean Sea off the coast of the Egyptian/Libyan border depicted via sun glitter [Scully Power, 1986]. The diameter of the eddies is roughly 10 km. (b) ERS-1 SAR image of 10-km spiral eddy in the Norwegian Coastal Current manifested via film-induced damping of the short Bragg waves. In this SAR image the maximum/minimum radar cross section (in dB) was reported to be $-9.5/-25$ [Johannessen *et al.*, 1996].

[26] In cases where no damping film material is present, the eddy features alter their expression into a bright radar modulation along the converging front as explained in section 2. An example of such a SAR image expression of a 10 km in diameter cyclonic eddy in the Norwegian Coastal Current is shown in Figure 6a that generally depicts the eddy boundary with a bright NRCS anomaly exceeding the background by up to 2–3 dB [Johannessen *et al.*, 1996].

[27] Eldevik and Dysthe [2002] recently put forward a conceptual model for the generation and evolution of spiral eddies. In meteorology, sharp fronts and cyclones are understood to be generated by the same baroclinic instability process [e.g., Garnier *et al.*, 1998]. As an unstable frontal wave evolves, there is both sharpening of horizontal gradients perpendicular to the wave and nonlinear windup of the wave to produce cyclones. Eldevik and Dysthe [2002] suggest that buoyant geostrophic jets in the upper ocean are prone to produce unstable frontal waves (“bad weather”) with wavelengths and growth rates consistent with the spirals. An example of the simulated surface flow pattern from their fine resolution (650 m horizontally, 5 m verti-

cally) numerical experiments is shown in Figure 6b. A frontal wave is seen to wind up nonlinearly to reveal cyclonic spirals. Both modeled and observed spiral eddies are associated with streaks of strong cyclonic shear and convergence. Owing to the convergence, the passive surface floating material accumulates to delineate the model eddies of Figure 6b. The experiments were done using the sigma-coordinate ocean model of Berntsen [2000].

[28] The surface current field (Figure 6b) with its zones of convergence and divergence (Figure 6c) obtaining strength of about 10^{-4} s^{-1} are used in the RIM to produce the NRCS field shown in Figure 6d. For a near-surface wind speed of 5 m/s from southwest (between cross-wind and downwind radar look direction) the NRCS contrasts along the eddy boundary reaches up to 2 dB. As emphasized in section 2, the enhanced wave breaking of intermediate waves in the vicinity of the zones of surface current convergence is the dominant source for the radar cross-section modulation and subsequent SAR image manifestation. This is confirmed by comparing the NRCS plot (Figure 6d) to the surface current divergence field (Figure 6c) as well as the distribution of the passive floating material (Figure 6b).

Figure 6. (a) ERS-1 SAR image expression of 10-km cyclonic eddy feature in the Norwegian Coastal Current; (b) modeled spiral eddies as traced out by passive floats and the surface velocity field; (c) corresponding surface divergence field; and (d) simulated radar cross section using the modeled current field (Figure 6b) as input.

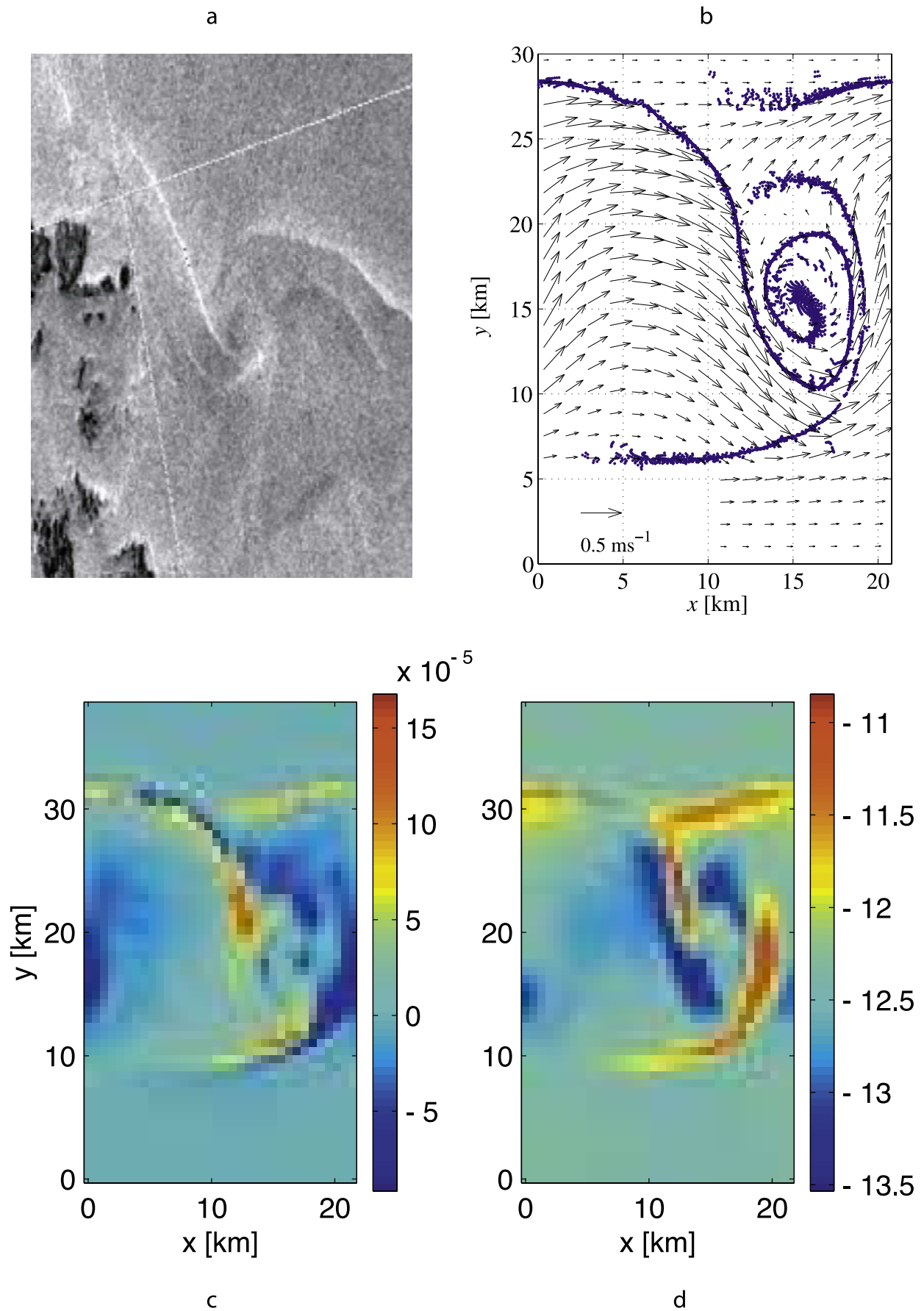


Figure 6

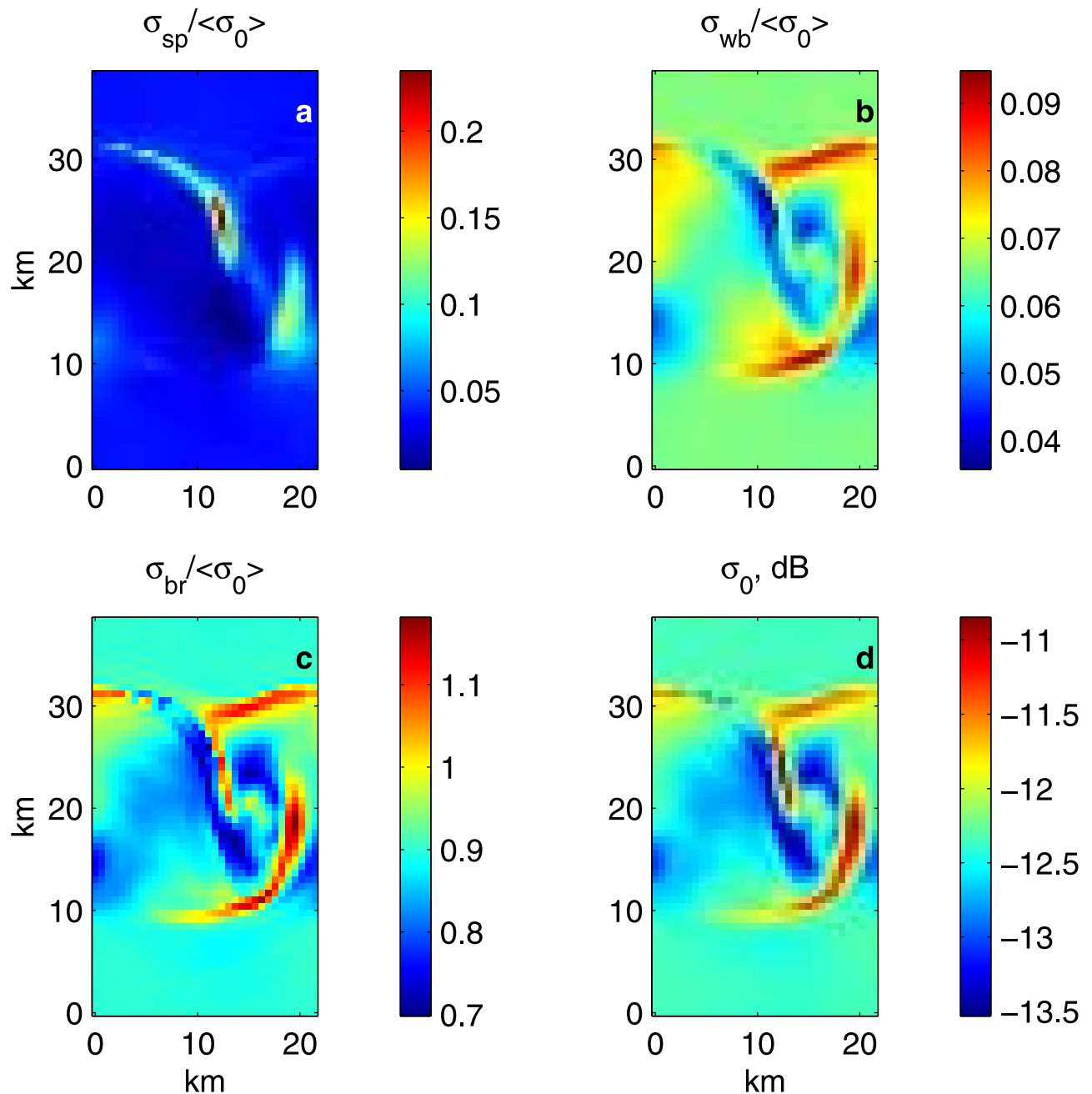


Figure 7. Relative importance of (a) specular, (b) wave breaking, and (c) Bragg scattering to (d) the total normalized radar cross section.

[29] The relative importance of specular scattering, wave breaking, and Bragg scattering to the total radar cross section is shown in Figure 7. With the exception of a narrow band in the vicinity of the convergence zone near the image center, the contribution from specular scattering (Figure 7a) is below 10% and hence negligible. Moreover, the direct contribution from the breaking zones (Figure 7b) to the NRCS can be ignored. Consequently, the indirect contribution from intermediate wave breaking via their influence on short wind waves dominates the surface roughness modulation, and thus Bragg-like scattering from the sea surface (Figure 7c) and the SAR image manifestation (Figure 7d). The total modulation depth across the

simulated cyclonic eddy is about 2 dB (Figure 7d) and compares reasonably well with the observed modulation depth of 2–3 dB (Figure 6a). It also reveals some bands of bright-dark anomaly patterns that in section 2 were found to be associated with the combined effect of convergence and divergence. These are not evident in the SAR image, nor is the image manifestation (Figure 6a) revealing any step-like impact from transformation of the MABL stratification due to sea surface temperature fronts. Hence this mechanism has not been included in the RIM simulation.

[30] Finally, we assess the impact of surfactants on the radar signature based on the fact that such short wave damping materials are accumulated by frontal convergence

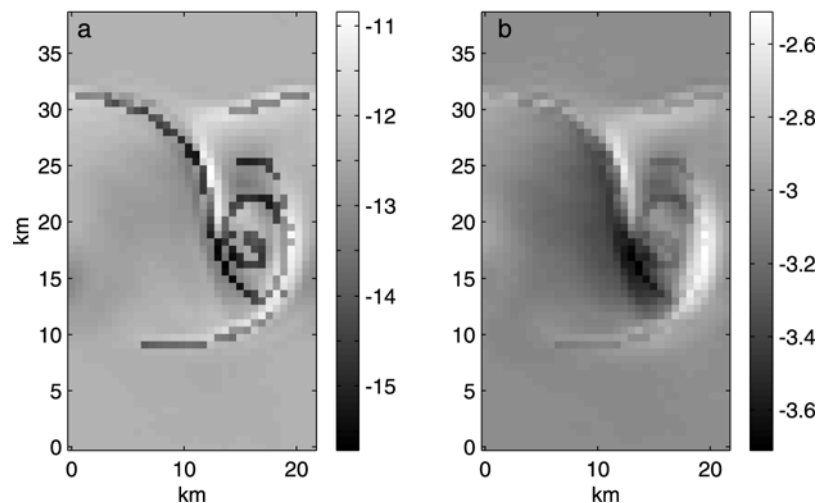


Figure 8. NRCS contrasts for the eddy current field in presence of surfactants. Wind speed (a) 5 m/s and (b) 15 m/s. Radar geometry is as for ERS SAR.

as clearly illustrated by the “numerical slick” in Figure 6b. The elasticity of the surfactants collected in the convergence zones is assumed to be a constant equal to 5 mN/m^2 [Ermakov *et al.*, 1992], and becomes effective for a given convergence strength. Any real transport of surfactants into the convergence zones is not taken into account. As discussed in Part 1, the surface film elasticity defines the effective viscosity coefficient, which in turn affects the wave spectrum. The corresponding model calculations of the radar signature are shown in Figure 8 for winds of 5 m/s (Figure 8a) and 15 m/s (Figure 8b). As expected, the surfactants significantly suppress the radar scattering. The 4-dB contrast of the dark features in Figure 8a which is related to the convergence zones attains a shape in very good agreement with the pattern in Figure 6b. Consequently, “clean” surface convergence zones are bright, while the presence of surfactants will turn the NRSC of the convergence zones darker. At stronger wind conditions, the surfactant impacts gradually disappear (Figure 8b). At this speed the impact of the wind forcing therefore overpowers the effect of surfactant damping. The magnitudes of the damping in these simulations are sensitive to the choice of elasticity. Hence they are not immediately comparable to the observed damping reported in Figure 5b, nor is it in the scope of the paper to address the fate of surfactants at higher winds. Note also that no simulation is done for 3 m/s as we enter into the threshold wind speed for a C-band radar [Donelan and Pierson, 1987].

[31] These interesting image simulations consistently extend the clear picture derived from the 1-D sensitivity experiments conducted at the end of section 2. Overall, they compare well with the SAR image expression of similar eddy features. The next category of RIM simulations addresses the mesoscale current variability corresponding to the Norwegian Coastal Current.

4. Mesoscale Variability

[32] The simulated mesoscale variability of the northward flowing Norwegian Coastal Current (NCC) is shown in Figure 9. The surface current and temperature fields contain

meanders and eddies ranging from 20–50 km. The temperature front varies from $2\text{--}4^\circ\text{C}$, while the magnitude of the corresponding surface current ranges from 0.7 to 0.9 m/s (Figure 9). This simulation builds on the Hybrid Coordinate Ocean Model (HYCOM) developed by Bleck [2002] that has been implemented for the North Sea and Skagerrak [Bertino *et al.*, 2004; Albretsen *et al.*, 2004] with a spatial resolution of about 2–4 km. The model is forced with atmospheric fields provided by the European Centre for Medium-Range Weather Forecasting (ECMWF).

[33] The subsurface structures associated with the meanders and eddies in the NCC are revealing irregular rises and drops of the pycnocline of more than 50 m over distances less than 5–10 km. This vertical density pattern can partly be connected with upwelling and downwelling events that are coupled with the areas of surface convergence and divergence.

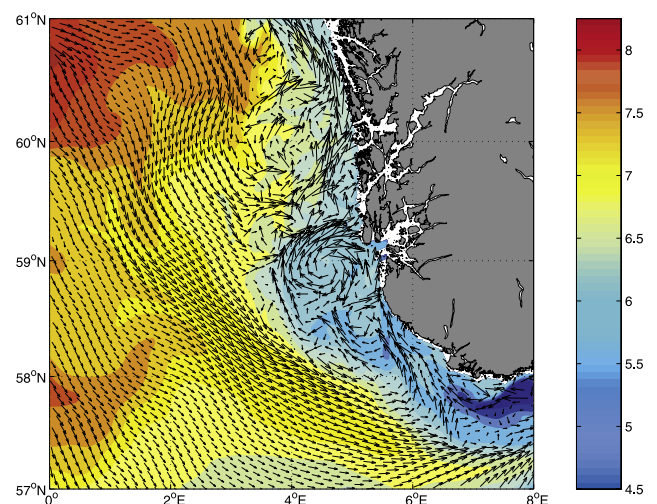


Figure 9. General surface circulation pattern and sea surface temperature structure of the modeled NCC. Maximum surface current (arrows) reaches up to 0.9 m/s. The color scale marks the sea surface temperature in degrees C.

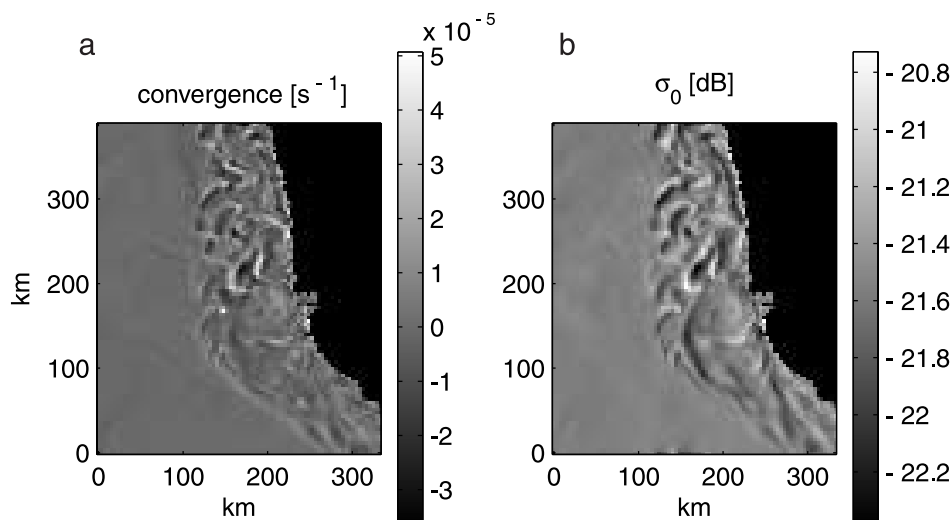


Figure 10. Comparison of (a) modeled surface current divergence and (b) simulated NRCS using the radar imaging model (Part 1).

[34] The ocean model fields have been systematically compared and evaluated with data from repeated ship cruises and demonstrate that the model is able to represent the general distribution of the major water masses, notably the saline Atlantic water and the fresh coastal water [Bertino *et al.*, 2004; Albretsen *et al.*, 2004]. Hence it is assumed that the baroclinic structure and corresponding current field are realistic. However, there has been no systematic validation of the mesoscale variability and simulated surface current patterns due to lack of data. On the basis of the promising results obtained in section 3, it is therefore highly interesting to examine how the mesoscale features within the NCC modulate the background surface roughness pattern that, in turn, might lead to SAR image expressions of the mesoscale variability.

[35] The mesoscale surface current field at 2 km resolution from Figure 9 is used to run the RIM. Moreover, a wind speed of 5 m/s at southerly (cross-wind) direction is used in consistence with the ECMWF field used to force HYCOM. The surface divergence map and the corresponding NRCS derived from the RIM are then compared in Figure 10. Note that the zones of convergence/divergence are bright (positive)/dark (negative) in Figure 10a. Maximum convergence reaches up to $4 \times 10^{-5} \text{ s}^{-1}$. This is almost an order of magnitude less than the convergence strength reported in section 3, and is most likely explained by the coarser (2–4 km) horizontal grid spacing in the NCC model. However, in spite of this relatively weak convergence strength, its pattern and orientation is in striking qualitative agreement with the simulated NRCS (Figure 10b) distribution that displays a total change of NRCS of about 1.5 dB. Although this is weaker than the 2-dB contrast reported in section 3 for a convergence of $2 \times 10^{-4} \text{ s}^{-1}$, it is again a clear confirmation that the NRCS anomalies mostly manifest the surface current divergence field.

[36] Capitalizing on this result, we proceed with an examination of how well the Envisat ASAR image expression of the NCC off the southwest coast of Norway obtained on 9 May 2003 (Figure 11a) can be interpreted using the RIM. The HYCOM realization of the surface

current and surface temperature distribution, displaying a nearly 2°C thermal front (Figure 11b), and the divergence field (Figure 11c) for the same day are also shown. The corresponding simulated NRCS for a 5 m/s wind normal to the radar look direction is shown in Figure 11d.

[37] The ASAR image expression (not corrected for the antenna pattern) is fairly complicated, with bands of bright and dark NRCS (Figure 11a) predominantly confined within the area occupied by the NCC (Figure 11b). The dominant wavelength of the modulation pattern is about 20–30 km with peak-to-background NRCS contrast ranging from 1 to 3 dB. In comparison, the mesoscale variability of the surface current within the NCC (Figure 11b) also attains a dominant length scale of 30 km. The current strength associated with these features ranges from 0.4 to 0.6 m/s and is thus weaker than for the case discussed above. Nevertheless, the divergence field (Figure 11c) reveals an abundance of zones of current convergence and divergence with magnitudes up to $2 \times 10^{-5} \text{ s}^{-1}$. As above, this is an order of magnitude less than for the spiral eddies discussed in section 3. In turn, the simulated NRCS obtains rather weak modulation depths up to 1 dB (Figure 11d). The structure and orientation of the modulations, on the other hand, agrees very well with the dominant pattern in the convergence and divergence field. The distinct drop in the level of simulated NRCS within the NCC arises from the transformation of the MABL over the colder coastal surface water. This expression is not pronounced in the ASAR image and may be attributed to the real MABL regime (different wind speed and sea surface temperature) and hence wind stress as suggested by the weaker thermal front of about 1.3°C found in a simultaneous, but partly cloud covered satellite Advanced Very-High Resolution Radiometer (AVHRR) thermal infrared image (not shown).

[38] Overall, this approach to interpreting SAR image expressions in the context of surface current convergence and divergence zones seems very promising. Combining numerical ocean models and the RIM thus appears as a powerful tool to either validate ocean models or quantify

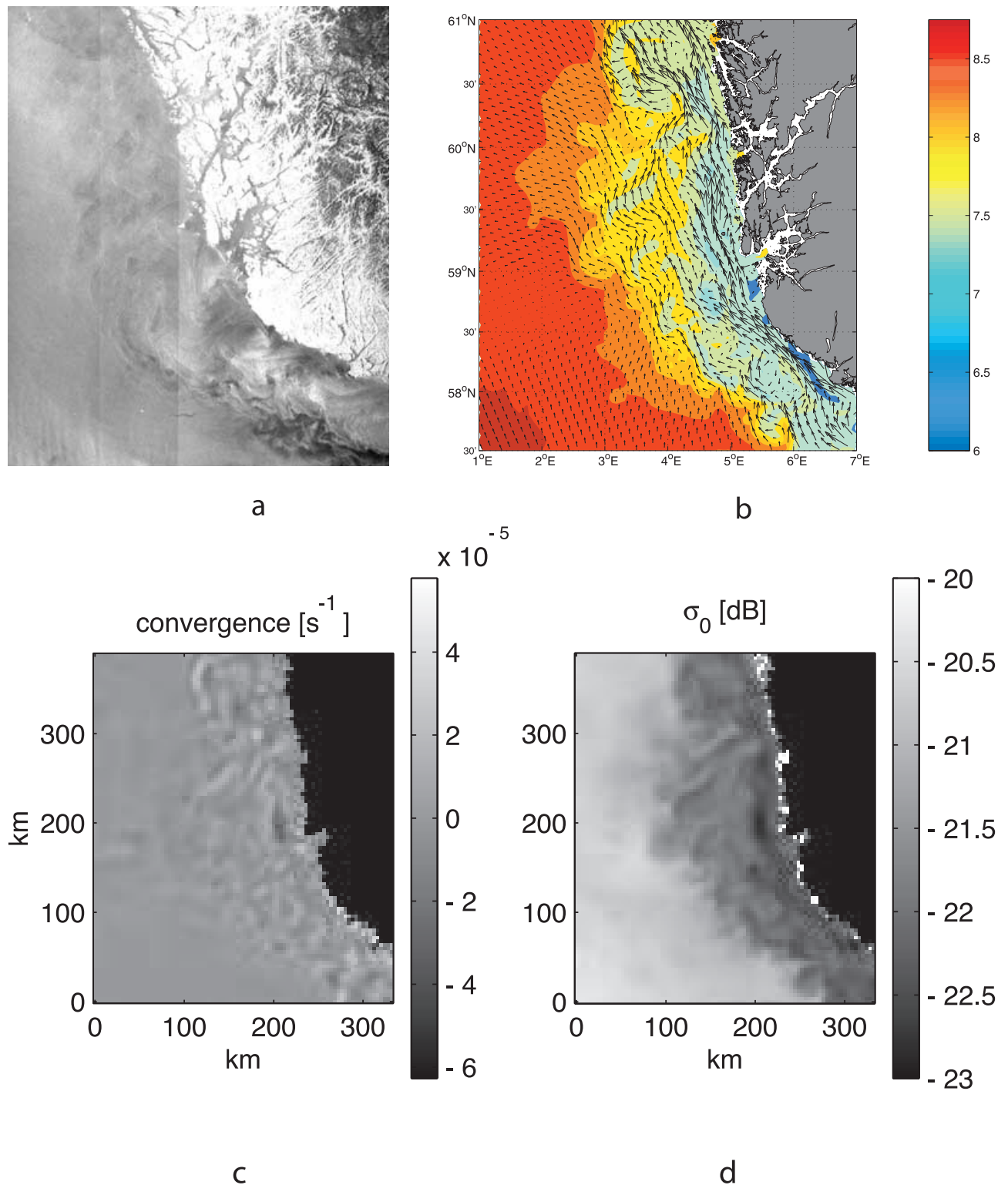


Figure 11. (a) ASAR image of the Norwegian Coastal Current off southwest coast of Norway on 9 May 2003. The corresponding (b) simulated surface current vector map and sea surface temperature in degrees C (see color scale), (c) divergence map, and (d) simulated NRCS (HH). The ASAR image is oriented along the descending flight track of the satellite and thus slightly skewed versus the model north-south orientation.

SAR images expressions of mesoscale current features as there are rarely sufficient quality and coverage by in situ data.

5. Concluding Remarks

[39] The ocean is rich in mesoscale dynamic features. Examples are meandering currents and eddy generation with distinct sea surface temperature fronts, the sporadic occurrence of filaments and jets, and wind-driven coastal upwelling and downwelling. Owing to a general lack of sufficient high-quality in situ observations, the understanding of how these dynamic features contribute to the complicated surface roughness modulation pattern often manifested in SAR images is incomplete. In turn, our ability to interpret and quantify surface current features imaged by SAR has not been adequately developed. Hitherto, the systematic use of SAR image observations for quantitative studies of the mesoscale ocean features has thus been hampered.

[40] A novel approach has therefore been pursued in this paper. A forward model is used that combines a new consistent radar imaging model (Part 1) with surface current and temperature fields obtained from two numerical 3-D ocean models at respectively 650 m and 2–4 km resolutions. These proxy data replace the desired high quality in situ data. They are probably still too coarse to fully explain and quantify the SAR image manifestations. However, the model fields are homogeneously sampled and allow us to examine the relation between the simulated SAR image and the upper layer ocean structures.

[41] A series of 1-D simulations were first undertaken to assess the RIM sensitivity to distinctive surface current and temperature conditions. The results emphasize the crucial role of current convergence and divergence that occur along meandering fronts and eddies as well as the wind direction versus the SAR look direction. In the case of convergence, the surface roughness modulation comes from the direct and indirect effects of the breaking of intermediate scale waves that takes place within the converging zone due to wave-current interaction. This, in turn, produces the sharp delta-like intensity changes in the radar cross section. In contrast, a pure shear current normal to the wind direction leads to no detectable departure from the background surface roughness and NRCS.

[42] For a meandering current front, zones of convergence and divergence are formed along the current shear. In this case, we obtain results that display bright (owing to convergence) and dark (divergence) NRCS anomalies of equal magnitude. Adding a sea surface temperature front to this case, that alters the surface stress, the NRCS profiles exhibit both delta-like and step-like changes. From the 1-D profile of the NRCS, it is therefore possible to distinguish surface roughness modulations due to currents only (e.g., the pure convergence associated with an internal wave case) from those resulting from both current and sea surface temperature changes (meandering fronts).

[43] By combining the new RIM with surface current fields from state-of-the-art ocean models, we further simulated the 2-D radar image manifestations of mesoscale fronts and eddies. The comparison with ERS-1 SAR and Envisat ASAR images for the case of eddies and meanders from the NCC is very promising. In particular, it is

concluded that: (1) the forward simulations consistently emphasize the crucial role of current convergence and divergence that occur along meandering fronts and eddies; (2) in the case of convergence, the surface roughness modulation comes from the (direct and indirect) effects of the breaking of intermediate scale waves that takes place within the converging zone owing to wave-current interaction; (3) in the presence of surfactants, efficient accumulation within the surface convergence zone can cause wave damping and suppression of the NRCS; (4) a pure shear current leads to no detectable departure from the background surface roughness and NRCS unless it meanders; and (5) the RIM includes the dominant interactive processes and their subsequent modulations of the surface roughness.

[44] More evaluations are certainly needed to consolidate these results. However, the consistent approach in the RIM can potentially enable the use of multiple sources of surface information, including 3-D ocean models, atmospheric forcing fields, and different satellite sensor wavelength and polarization characteristics, as well as in situ devices (like for instance HF radars). Note also that a growing number of experimental SAR satellites are planned to be launched within the next few years (e.g., TerraSAR X, COSMO-SkyMed) that will complement the currently operating C-band Radarsat and Envisat ASAR. Future work shall also be directed toward the combination of this approach with the Doppler centroid information retrieved in SAR systems [e.g., Chapron *et al.*, 2004, 2005; Kerbaol and Collard, 2005]. Overall, we therefore conclude that these promising results will open new opportunities for more systematic studies of mesoscale ocean variability based on SAR in the coming years.

[45] **Acknowledgments.** Core support for this study was provided by the EU funded 5th Framework Program (FP 5) project MARS AIS (contract EVG1-CT-2000-00029), the SARMIS project financed under the bilateral EU-Russia support agreement (INTAS contract 00-598), and the MONCOZE and ProClim projects funded by the Norwegian Research Council (contract 143559/431 and 155923/700). Moreover, the Norwegian Spacecenter has supported the work under contract JOP.8.3.3.06.01.1. In addition, the authors also acknowledge the support of ESA under the ESA-IAF project on “GMES Networking with Russia and Ukraine” and in providing the SAR images used in this paper.

References

- Albretsen, J., N. Winther, H. Soiland, and L. P. Røed (2004), Models in MONCOZE, *Rep. 14/2004*, Norw. Meteorol. Inst., Oslo.
- Alpers, W. (1985), Theory of radar imaging of internal waves, *Nature*, *314*, 245–247.
- Alpers, W., and I. Hennings (1984), A theory of the imaging mechanism of underwater bottom topography by real and synthetic aperture radar, *J. Geophys. Res.*, *89*(C6), 10,529–10,546.
- Apel, J. R. (1994), An improved model of the ocean surface wave vector spectrum and its effects on radar backscatter, *J. Geophys. Res.*, *99*(C8), 16,269–16,291.
- Berntsen, J. (2000), User guide for a mode split sigma-coordinate numerical ocean model, version 1.0, *Rep. 135*, Dep. of Appl. Math., Univ. of Bergen, Bergen, Norway.
- Bertino, L., N. Winther, and J. A. Johannessen (2004), Real-time marine monitoring systems: Forecasting ocean and regional sea-state, *Hydro Int.*, *8*(5), 40–45.
- Bleck, R. (2002), An oceanic general circulation model framed in hybrid isopycnal-Cartesian coordinates, *Ocean Modell.*, *4*, 55–88.
- Chapron, B., F. Collard, and V. Kerbaol (2004), Satellite synthetic aperture radar sea surface Doppler measurements, in *Proceedings of the Second Workshop Coastal and Marine Applications of SAR, ESA SP-565*, pp. 133–141, Eur. Space Agency, Paris.
- Chapron, B., F. Collard, and F. Ardhuin (2005), Direct measurements of ocean surface velocity from space: Interpretation and validation, *J. Geophys. Res.*, *110*, C07008, doi:10.1029/2004JC00280.

- Dokken, S. T., and T. Wahl (1996), Observations of spiral eddies along the Norwegian coast in ERS SAR images, *Rep. 96/01463*, Norw. Def. Res. Estab., Kjeller, Norway.
- Donelan, M. A., and W. J. Pierson (1987), Radar scattering and equilibrium ranges in wind-generated waves with application to scatterometry, *J. Geophys. Res.*, *92*(C5), 4971–5029.
- Eldevik, T., and K. B. Dysthe (2002), Spiral eddies, *J. Phys. Oceanogr.*, *32*, 851–869.
- Ermakov, S. A., S. G. Salashin, and A. R. Panchenko (1992), Film slicks on the sea surface and some mechanisms of their formation, *Dyn. Atmos. Oceans*, *16*, 279–304.
- Font, J., S. Rousseau, B. Shirasago, E. Garcia-Gorri, and R. L. Haney (2002), Mesoscale variability in the Alboran Sea: Synthetic aperture radar imaging of frontal eddies, *J. Geophys. Res.*, *107*(C6), 3059, doi:10.1029/2001JC000835.
- Fu, L. L., and R. H. Stewart (1983), Some examples of detection of oceanic mesoscale eddies by the Seasat synthetic aperture radar, *J. Geophys. Res.*, *88*(C3), 1844–1852.
- Garnier, E., O. Métais, and M. Lesieur (1998), Synoptic and frontal-cyclone scale instabilities in baroclinic jet flows, *J. Atmos. Sci.*, *55*, 1316–1335.
- Johannessen, J., R. Shuchman, G. Digranes, D. Lyzenga, W. Wackerman, O. Johannessen, and P. Vachon (1996), Coastal ocean fronts and eddies imaged with ERS-1 synthetic aperture radar, *J. Geophys. Res.*, *101*(C3), 6651–6667.
- Johannessen, O. M., E. Korsbakken, P. Samuel, A. D. Jenkins, and H. Espedal (1997), COAST WATCH: Using SAR imagery in an operational system for monitoring coastal currents, wind, surfactants and oil spills, in *Operational Oceanography: The Challenge for European Co-operation*, *Oceanogr. Ser.*, vol. 62, edited by J. H. Stel, pp. 234–242, Elsevier, New York.
- Kerbaol, V., and F. Collard (2005), SAR-derived coastal and marine applications: From research to operational products, *IEEE Journal of Oceanic Engineering*, in press.
- Kudryavtsev, V., and J. Johannessen (2004), On effect of wave breaking on spectrum of short wind waves, *Geophys. Res. Lett.*, *31*, L20310, doi:10.1029/2004GL020619.
- Kudryavtsev, V., D. Hauser, G. Caudal, and B. Chapron (2003a), A semi-empirical model of the normalized radar cross-section of the sea surface: 1. The background model, *J. Geophys. Res.*, *108*(C3), 8054, doi:10.1029/2001JC001003.
- Kudryavtsev, V., D. Hauser, G. Caudal, and B. Chapron (2003b), A semi-empirical model of the normalized radar cross-section of the sea surface: 2. Radar modulation transfer function, *J. Geophys. Res.*, *108*(C3), 8055, doi:10.1029/2001JC001004.
- Kudryavtsev, V., D. Akimov, and O. M. Johannessen (2003c), Radar imaging of the ocean mesoscale variability, *Earth Observations from Space*, vol. 2, pp. 27–46, Russ. Acad. of Sci., Moscow.
- Kudryavtsev, V., D. Akimov, J. A. Johannessen, and B. Chapron (2005), On radar imaging of current features: 1. Model and comparison with observations, *J. Geophys. Res.*, C07016, doi:10.1029/2004JC002505.
- Lyzenga, D. R. (1996), Effects of wave breaking on SAR signatures observed near the edge of the Gulf Stream, in *Proceedings of International Geoscience and Remote Sensing Symposium*, pp. 908–910, IEEE Press, Piscataway, N. J.
- Lyzenga, D. R., and J. R. Bennett (1988), Full-spectrum modeling of synthetic aperture radar internal wave signature, *J. Geophys. Res.*, *93*(C10), 12,345–12,354.
- Lyzenga, D. R., G. Marmorino, and J. A. Johannessen (2004), Ocean currents and current gradients, in *Synthetic Aperture Radar Marine Manual*, edited by C. R. Jackson and J. R. Apel, chap. 8, pp. 207–220, Natl. Oceanic and Atmos. Admin., Silver Spring, Md.
- Munk, W., L. Armi, K. Fischer, and F. Zachariasen (2000), Spirals on the sea, *Proc. R. Soc. London, Ser. A*, *456*, 1217–1280.
- Phillips, O. M. (1985), Spectral and statistical properties of the equilibrium range in wind-generated gravity waves, *J. Fluid Mech.*, *156*, 505–531.
- Romeiser, R., and W. Alpers (1997), An improved composite surface model for the radar backscattering cross section of the ocean surface: 2. Model response to surface roughness variations and the radar imaging of underwater bottom topography, *J. Geophys. Res.*, *102*(C11), 25,251–25,267.
- Romeiser, R., S. Ufermann, and W. Alpers (2001), Remote sensing of oceanic current features by synthetic aperture radar-achievements and perspectives, *Ann. Telecommun.*, *11/12*, 661–671.
- Scully-Power, P. (1986), Navy oceanographer shuttle observations, STS 41-G: Mission report, *Tech. Rep. NUSC TD 7611*, 71 pp., Nav. Underwater Syst. Cent., Newport, R. I.
- D. Akimov, Nansen International Environmental and Remote Sensing Center, St. Petersburg, Russia.
- B. Chapron, Institute Francais de Recherche pour l'Exploitation de la Mer, Plouzane, France.
- T. Eldevik, J. A. Johannessen, and N. Winther, Nansen Environmental and Remote Sensing Center, Thormohlensgate 47, Bergen, N-5006 Norway. (johnny.johannessen@nersc.no)
- V. Kudryavtsev, Nansen International Environmental and Remote Sensing Center, St. Petersburg, Russia.